The Astrophysical Journal, 978:145 (11pp), 2025 January 10 https://doi.org/10.3847/1538-4357/ad9b97

Prospects for Observing High-redshift Radio-loud Quasars in the SKA Era: Paving the Way for 21 cm Forest Observations

Qi Niu[1], Yichao Li[1], Yidong Xu[2,3], Hong Guo[4], and Xin Zhang[1,5,6]
[1] Liaoning Key Laboratory of Cosmology and Astrophysics, College of Sciences, Northeastern University, Shenyang 110819, People's Republic of China; zhangxin@mail.neu.edu.cn
[2] National Astronomical Observatories, Chinese Academy of Sciences, Beijing 100101, People's Republic of China; xuyd@nao.cas.cn
[3] Key Laboratory of Radio Astronomy and Technology, Chinese Academy of Sciences, Beijing 100101, People's Republic of China
[4] Shanghai Astronomical Observatory, Chinese Academy of Sciences, Shanghai 200030, People's Republic of China
[5] National Frontiers Science Center for Industrial Intelligence and Systems Optimization, Northeastern University, Shenyang 110819, People's Republic of China
[6] MOE Key Laboratory of Data Analytics and Optimization for Smart Industry, Northeastern University, Shenyang 110819, People's Republic of China
Received 2024 August 01; revised 2024 November 22; accepted 2024 December 05; published 2025 January 8

Abstract

The 21 cm forest is a sensitive probe for the early heating process and small-scale structures during the epoch of reionization (EOR), to be realized with the upcoming Square Kilometre Array (SKA). Its detection relies on the availability of radio-bright background sources, among which the radio-loud quasars are very promising, but their abundance during the EOR is still poorly constrained due to limited observations. In this work, we use a physics-driven model to forecast future radio-loud quasar observations. We fit the parameters of the model using observational data of high-redshift quasars. Assuming Eddington accretion, the model yields an average lifetime of $t_q \sim 10^{5.5}$ yr for quasars at $z \sim 6$, consistent with recent results obtained from quasar proximity zone observation. We show that if the radio-loud fraction of quasars evolves with redshift, it will significantly reduce the abundance of observable radio-loud quasars in the SKA era, making 21 cm forest studies challenging. With a constant radio-loud fraction, our model suggests that a 1 yr sky survey conducted with SKA-LOW has the capability to detect approximately 20 radio-loud quasars at $z \sim 9$, with sufficient sensitivity to resolve individual 21 cm forest lines.

Unified Astronomy Thesaurus concepts: Quasars (1319); Radio loud quasars (1349); Reionization (1383); H I line emission (690)

1. Introduction

The origin and evolution of stars, galaxies, and supermassive black holes in the Universe are among the great unsolved mysteries of cosmology. Unveiling these enigmas requires probing the first billion years of cosmic history. The exploration of the cosmic dawn and the epoch of reionization (EOR) primarily rely on the use of the 21 cm hyperfine structure spectral line of neutral hydrogen atoms. Detecting the 21 cm cosmological signal is extremely challenging, but once a breakthrough is achieved, its scientific significance is enormous (S. R. Furlanetto et al. 2006; M. F. Morales & J. S. B. Wyithe 2010; J. R. Pritchard & A. Loeb 2012; Y. Xu & X. Zhang 2020).

Probing the 21 cm signals of hydrogen atoms in the early Universe mainly relies on the cosmic microwave background as the background radio source, detecting the absorption signals from the dark ages and the cosmic dawn, or the emission signals during the EOR when the gas is heated up by the early galaxies. Due to cosmic expansion, these 21 cm signals have been redshifted to a low-frequency radio band, typically requiring low-frequency radio telescopes for observation. Currently, experiments to detect the cosmic dawn and EOR are in full swing, including experiments to detect the sky-averaged spectrum of the 21 cm signal during the cosmic dawn, such as the Experiment to Detect the Global EoR Signature (J. D. Bowman et al. 2018), the Shaped Antenna measurement of the background RAdio Spectrum (S. Singh et al. 2018), the Hongmeng Project (X. Chen et al. 2023), the Mapper of the ionizing intergalactic medium (IGM) Spin Temperature (R. A. Monsalve et al. 2024), the Radio Experiment for the Analysis of Cosmic Hydrogen (E. de Lera Acedo et al. 2022), Probing Radio Intensity at high-Z from Marion (L. Philip et al. 2019), the Large-aperture Experiment to Detect the Dark Age (D. C. Price et al. 2018), Probing ReionizATion of the Universe using Signal from Hydrogen (M. Sathyanarayana Rao et al. 2023), the Dark Ages Polarimeter Pathfinder,[7] and the High-Z All-Sky Spectrum Experiment (O. Navros 2022). Additionally, there are experiments to detect the 21 cm power spectrum during the EOR, such as the Low-Frequency Array (LOFAR; A. H. Patil et al. 2017), the Murchison Widefield Array (MWA; S. J. Tingay et al. 2013), the Precision Array for Probing the Epoch of Reionization (A. R. Parsons et al. 2010), the Hydrogen Epoch of Reionization Array (D. R. DeBoer et al. 2017), the upgraded Giant Metrewave Radio Telescope (Y. Gupta et al. 2017), and the New Extension in NanÃğay Upgrading LOFAR (S. Munshi et al. 2024).

In particular, the Square Kilometer Array (SKA; M. Huynh & J. Lazio 2013) under construction will be the largest radio telescope to date. It has a large field of view, a broad band, and an ultrahigh sensitivity, capable of taking tomographic images of IGM (L. Koopmans et al. 2015), which will reveal more detailed information of the EOR and make an important contribution to understanding the origin of cosmic structures.

In addition to these three measurement modes, another method of observing 21 cm signals is known as the 21 cm forest. If there are radio-bright point sources at the EOR, such

[7] https://www.colorado.edu/ness/sites/default/files/attached-files/dapper_mission_fact_sheet_rev_may_2019.pdf

as radio-loud quasars and radio afterglows of high-redshift gamma-ray bursts, neutral clumps along the line of sight would create individual absorption lines on the source spectra, forming forest-like features called the 21 cm forest (in analogy to the Lyα forest; C. L. Carilli et al. 2002; S. R. Furlanetto & A. Loeb 2002; S. R. Furlanetto 2006; Y. Xu et al. 2009, 2010). The observation of 21 cm forest is of great value for studying the properties of the IGM, as it is highly sensitive to the heating process caused by the formation of early galaxies (Y. Xu et al. 2009; Y. Xu et al. 2011; B. Ciardi et al. 2013), and also for constraining the abundance of small-scale structures, so as to measure the properties of dark matter (DM; H. Shimabukuro et al. 2014, 2020; K. Kadota et al. 2021). Recently, it was found that the one-dimensional cross power spectrum measurement of the 21 cm forest can be used to help extract faint 21 cm signals, and can also further measure the properties of DM and the early galaxies simultaneously (Y. Shao et al. 2023).

The utilization of the 21 cm forest method is presently limited by three factors. First, attaining the sensitivity necessary for detecting the 21 cm forest poses a challenge. Current radio telescopes, such as LOFAR and MWA, lack the capability of conducting extensive detection deep into the EOR (B. Ciardi et al. 2013; S. Chatterjee et al. 2024). The anticipated completion of SKA in the near future will significantly mitigate this existing detection challenge (B. Ciardi et al. 2015; L. Koopmans et al. 2015; T. Šoltinský et al. 2021). The vast effective aperture of SKA-LOW will empower us to detect the reionization process with unparalleled sensitivity. Second, there is a lack of an analytical model to connect physical parameters (such as DM mass and IGM temperature, etc.) with the 21 cm forest observational signals, making it difficult to carry out observational constraints on physical parameters (note that parameter inference based on large-scale simulations is extremely resource-intensive). To address this issue, we can consider constructing an analytical model. Alternatively, it is also possible to utilize methods based on deep learning. Recently, T.-Y. Sun et al. (2024) have developed a set of deep-learning-based data generation and likelihood-free parameter inference methods to simultaneously address the issues of the absence of an analytical model and small-scale non-Gaussianity. Third, the 21 cm forest necessitates high-redshift radio point sources as backgrounds. Owing to observational limitations, our understanding of the abundance of high-redshift radio sources remains limited, constituting the foremost uncertainty in the application of the 21 cm forest.

Quasars are one of the brightest sources in the Universe, with about 10% of quasars exhibiting strong radio emissions (D. Stern et al. 2000; Z. Ivezić et al. 2002; E. Bañados et al. 2015; A. J. Gloudemans et al. 2021; Y. Liu et al. 2021). These radio-loud quasars serve as ideal background sources for 21 cm forest. With the continuous advancement of optical and near-infrared detection, the frontier of observing quasar redshift has reached 7.64 (F. Wang et al. 2021). However, there are only 9 quasars observed with redshift exceeding 7, and 14 radio-loud quasars observed with redshift exceeding 6 (I. D. McGreer et al. 2006; C. J. Willott et al. 2010; E. Bañados et al. 2015, 2021; L. Ighina et al. 2021, 2023; Y. Liu et al. 2021; A. J. Gloudemans et al. 2022; E. Bañados et al. 2023; R. Endsley et al. 2023; E. Bañados et al. 2024). Fortunately, the successful operation of the James Webb Space Telescope (JWST) has greatly enhanced our ability to detect high-redshift active galactic nuclei (AGNs). A number of high-redshift AGNs or AGN candidates have already been reported through observations with the JWST (e.g., A. D. Goulding et al. 2023; Y. Harikane et al. 2023; D. D. Kocevski et al. 2023; R. L. Larson et al. 2023; H. Übler et al. 2023; J. Lyu et al. 2024), making the search for AGNs at even higher redshifts possible. During the deeper reionization of epochs at higher redshifts, it is crucial to obtain theoretical estimates to determine whether there are sufficient radio-loud quasars available for 21 cm forest research.

To predict the abundance of high-redshift radio-loud quasars, Z. Haiman et al. (2004; hereafter H04) developed a model driven by physical processes. By assuming a correspondence between supermassive black holes (SMBHs) and halos, as well as employing the Eddington limit for accretion, this model successfully derived the abundance of radio-loud quasars consistent with observational data. After nearly two decades of equipment upgrades and observational data accumulation, we have gained further understanding of some of the physical and statistical properties of high-redshift quasars (e.g., Z. Shang et al. 2011; J. C. Runnoe et al. 2012; Y. Matsuoka et al. 2018; K. Shimasaku & T. Izumi 2019; J. Yang et al. 2021; Y. Matsuoka et al. 2023; T. Šoltinský et al. 2023; P. M. Keller et al. 2024). Currently, some assumptions of the H04 model are challenged by observational data, requiring reasonable extensions and calibrations to fit the actual distribution of high-redshift quasars. This paper aims to update this model and make reasonable predictions for radio-loud quasar observations in the SKA era.

This paper is structured as follows. In Section 2, we describe the construction of the model and its calibration using high-redshift observational data. In Section 3, we present predictions for future SKA-LOW observations of radio-loud quasars and discuss the impact of currently poorly constrained parameters on the results. In Section 4, we give a summary of our findings and their implications. For this study, we presume the ΛCDM model and use the cosmological parameters measured by Planck 2018 (Planck Collaboration et al. 2020): $\Omega_m = 0.3111$, $\Omega_\Lambda = 0.6889$, $\Omega_b = 0.04897$, $h = 0.6766$, $\sigma_8 = 0.8102$, and $n_s = 0.9665$.

2. Method

In this section, we present the construction process of the model and discuss the rationality of some physical assumptions, eventually providing a calibrated model suitable for predicting high-redshift ($z \sim 6$) quasar observations. The calibration of the model uses quasar UV luminosity functions data at $z \sim 6$ (Y. Matsuoka et al. 2018) and $z \sim 6.8$ (Y. Matsuoka et al. 2023), as well as the black hole masses and the DM halo masses they inhabit obtained from 49 quasars at $z \sim 6$ (K. Shimasaku & T. Izumi 2019).

2.1. Halo Mass Function

Quasars are powered by SMBHs. Therefore, we first need to estimate the abundance of SMBHs at the centers of galaxies. We assume that the SMBH population traces DM halos, and the distribution of DM halos follows the Sheth–Tormen form (R. K. Sheth & G. Tormen 2002), i.e.,

$$\frac{dn}{dM_{\rm halo}} = f(\sigma, z) \quad \frac{\rho_0}{M_{\rm halo}} \frac{d \quad \ln(\sigma^{-1})}{dM_{\rm halo}}, \tag{1}$$

where

$$f(\sigma, z) = 0.322\sqrt{\frac{3}{2\pi}}\frac{\delta_c}{\sigma}\left(1 + \left(\frac{4\sigma^2}{3\delta_c{}^2}\right)^{0.3}\right)\exp\left[-\frac{3\delta_c{}^2}{8\sigma^2}\right]. \quad (2)$$

Here $\delta_c = 1.686$ is the critical overdensity for spherical collapse, and ρ_0 is the background density. σ is the rms of density fluctuations,

$$\sigma^2(M, z) = \sigma^2(R_{\rm sph}, z) = \int_0^\infty \frac{dk}{2\pi^2}k^2P(k, z)\left[\frac{3j_1(kR_{\rm sph})}{kR_{\rm sph}}\right]^2, \quad (3)$$

where $j_1(x) = (\sin x - x \cos x)/x^2$, $R_{\rm sph}$ is the comoving radius related to mass M by $M = 4\pi\rho_{\rm m}R_{\rm sph}^3/3$. The cosmological power spectrum $P(k, z)$ is calculated using the fitting form of D. J. Eisenstein & W. Hu (1999). Since we are discussing quasars during the cosmic reionization when DM halos had not undergone large-scale mergers, this assumption is reasonable.

2.2. Halo–SMBH Mass Relation

By assuming that the radiation feedback and outflows of quasars determine the size of black holes, we can obtain the scaling relationship between black hole mass and DM halo mass (M. G. Haehnelt et al. 1998; J. Silk & M.J. Rees 1998; J. S. B. Wyithe & A. Loeb 2003). The mass scaling relation is expressed as (Equation (4) in J. S. B. Wyithe & A. Loeb 2003)

$$M_{\rm BH} = A\left(\frac{M_{\rm halo}}{1.5 \times 10^{12}M_\odot}\right)^{5/3}\left[\frac{\xi(z)}{\Omega_m}\right]^{5/6}(1+z)^{5/2}M_\odot, \quad (4)$$

where $M_{\rm BH}$ is the black hole mass, $M_{\rm halo}$ is the DM halo mass, A is the amplitude parameter, $\xi(z)$ is the dimensionless parameter related to redshift z, and $\xi(z) \simeq \Omega_m$ for $z \geqslant 6$.

The scaling relation between $M_{\rm BH}$ and $M_{\rm halo}$ in Equation (4) is derived from a physically motivated model combining the $M_{\rm BH}$–$\sigma_{\rm h}$ relation ($M_{\rm BH} \propto {\sigma_{\rm h}}^\beta$, where $\sigma_{\rm h}$ is halo velocity dispersion) and the halo virialization ($M_{\rm halo} \propto \sigma_{\rm h}^3$). The radiation-driven model proposed by J. Silk & M.J. Rees (1998) predicts $M_{\rm BH} \propto \sigma_{\rm h}^5$, while the momentum-driven model proposed by A. King (2003) predicts $M_{\rm BH} \propto \sigma_{\rm h}^4$. The results obtained from observations of the nearby Universe lie between these two models (e.g., L. Ferrarese & D. Merritt 2000; K. Gebhardt et al. 2000; K. Gültekin et al. 2009; J. Kormendy & L. C. Ho 2013; N. J. McConnell & C.-P. Ma 2013), which are considered as evidence of the coevolution of galaxies and SMBHs. However, this relation has not been thoroughly studied at high redshifts. To better predict the relation for high-redshift quasars, we use the SMBH and halo masses obtained from observational data of 49 quasars at $z \sim 6$ (K. Shimasaku & T. Izumi 2019). We tried to treat the first power-law index in Equation (4) as a free parameter and found that the 49 data points favor a notably low power-law index of ~0.22. Such a low index shows a large discrepancy from low-redshift observations, and it could hardly be explained by physically motivated models. Considering the large intrinsic scatter and the large error bars of the limited sample, we attribute this discrepancy to observational systematics and incompleteness at high redshifts, which prevent us from obtaining a reliable index estimate from these data. Due to the limited understanding of the evolution of SMBHs at high redshifts, in this study, we follow the choice of H04 and adopt a fixed index of 5/3.

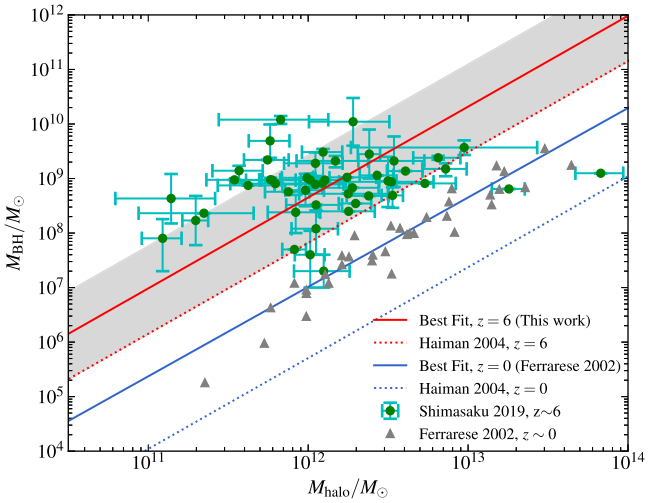

Figure 1. $M_{\rm halo}$–$M_{\rm BH}$ relation. The red lines represent the fitting results at $z = 6$, and the blue lines represent the results for $z = 0$. Solid lines represent observational fitting, while dashed lines represent the mass relation used by H04. The shaded area represents the intrinsic scatter $\sigma_{\rm in}$. The gray triangular data points are from L. Ferrarese (2002), and the green data points are from K. Shimasaku & T. Izumi (2019).

We note that the $M_{\rm BH}$–$\sigma_{\rm bulge}$ relation measured in the nearby Universe exhibits intrinsic scatter (e.g., J. Kormendy & L. C. Ho 2013), which will naturally propagate to the $M_{\rm halo}$–$M_{\rm BH}$ relation we are fitting. Therefore, we assume that the high-redshift data contain intrinsic scatter following a Gaussian distribution $\mathcal{N}(0, \sigma_{\rm in})$ in the logarithmic space, and construct the likelihood function as

$$\mathcal{L}(A, \sigma_{\rm in}) = \prod_{i=1}^N \frac{1}{\sqrt{2\pi(\sigma_{m,i}^2 + \sigma_{\rm in}^2)}} \times \exp\left(-\frac{(\log(M_{{\rm BH},i}) - \log(M_{{\rm model},i}(A)))^2}{2(\sigma_{m,i}^2 + \sigma_{\rm in}^2)}\right), \quad (5)$$

where A is the amplitude parameter defined in Equation (4), $\sigma_{\rm in}$ is the intrinsic scatter, $\sigma_{m,i}$ is the measurement error of each data point, $M_{{\rm BH},i}$ is the black hole mass of each data point, and $M_{{\rm model},i}$ is the black hole mass obtained from Equation (4). We obtain the best-fit values of the amplitude parameter A and the intrinsic scatter $\sigma_{\rm in}$ using the maximum likelihood estimation method, and the results are shown in Figure 1 as the red line with the shaded area being the 1σ range ($\log(A) = 6.8 \pm 0.81$), the reduced $\chi^2 \simeq 1.02$. We found that the best-fit amplitude parameter $A = 10^{6.8}$ is approximately 7 times the amplitude used by H04. As the intrinsic scatter is well-characterized by a normal distribution, the fitting result of Equation (4) represents the theoretical mean. For simplicity, we exclusively use Equation (4) with the fitted amplitude in subsequent calculations, without accounting for intrinsic scatter.

We note that H04 used quasar luminosity function data at $z \gtrsim 3$ to fit the amplitude parameter, with the average quasar lifetime fixed at 2×10^7 yr. However, the results obtained did not match the observations of the local Universe and those at $z = 6$ (see Figure 1). Note that recent studies on quasar lifetimes suggest shorter lifetimes (A.-C. Eilers et al. 2017, 2021; K. A. Morey et al. 2021), and in our analysis, the average quasar lifetime is treated as a variable and is

constrained by high-redshift luminosity function data (see Section 2.4).

2.3. Accretion Rate and Optical Luminosity

We assume that the average Eddington ratio $\lambda_{\rm Edd}$ for high-redshift quasars is 1, indicating Eddington accretion. Although the average accretion rate of quasars in the local Universe is much lower than Eddington accretion, recent high-redshift observations suggest that the average Eddington ratio of early quasars is close to 1 (J. Yang et al. 2021). Additionally, we note that to explain the formation of SMBHs represented by the observed high-redshift quasars, some studies have adopted models of sustained mild super-Eddington accretion (e.g., F. Pacucci et al. 2015; W. Li et al. 2023) or chaotic accretion (e.g., K. Zubovas & A. King 2021). The results of A. Lupi et al. (2024) indicate that super-Eddington accretion can also persist for a long time. Based on the above observation and simulation results, we believe our assumption is reasonable.

Once we determine the Eddington ratio, we can calculate the optical luminosity of quasars. Assuming a quasar has an average Eddington ratio of $\lambda_{\rm Edd}$ over its lifetime, we can get the bolometric luminosity as

$$L_{\rm bol} = \lambda_{\rm Edd} L_{\rm Edd}, \tag{6}$$

where $L_{\rm Edd}$ is the Eddington luminosity. As discussed above, we adopt $\lambda_{\rm Edd} = 1$ for most of our calculations. We will also discuss the case with $\lambda_{\rm Edd} = 1.2$.

For the quasar bolometric luminosity corrections, we use the results from J. C. Runnoe et al. (2012) (their Equations (11) and (13)):

$$\log(L_{\rm bol}) = \log(0.75) + 4.89 + 0.91 \times \log(5100 L_{5100}). \tag{7}$$

We adopt the average spectral energy distribution (SED) from Z. Shang et al. (2011) to calculate the luminosity relationship between different optical bands:

$$\lambda F_\lambda(1450\ \text{Å}) \simeq 1.86 \quad \lambda F_\lambda(5100\ \text{Å}), \tag{8}$$

$$\lambda F_\lambda(2500\ \text{Å}) \simeq 1.76 \quad \lambda F_\lambda(5100\ \text{Å}), \tag{9}$$

$$\lambda F_\lambda(4400\ \text{Å}) \simeq 1.11 \quad \lambda F_\lambda(5100\ \text{Å}), \tag{10}$$

where $\lambda F_\lambda(\lambda)$ is the rest-frame spectral flux at wavelength λ.

2.4. Duty Cycle of Quasar Phase

Through the halo mass function and the halo–SMBH mass relation, we have obtained the black hole mass function. However, not all black holes are in the quasar phase at the same time. We need to estimate the proportion of black holes that are in the quasar phase, which is the duty cycle. We estimate the duty cycle as

$$D_{\rm q} = \frac{t_{\rm q}}{t_{\rm H}(z)}, \tag{11}$$

where $t_{\rm q}$ is the average lifetime of quasars, and $t_{\rm H}(z)$ is the age of the Universe at redshift z.

By combining the black hole mass function with Equations (6)–(8) and (11), we can calculate the quasar luminosity function (QLF; the comoving number density of quasars per unit of magnitude) as

$$\Phi(M_{1450}, z) = \frac{dn_{\rm q}}{dM_{1450}} = D_{\rm q} \frac{dn_{\rm BH}}{dM_{\rm BH}} \frac{dM_{\rm BH}}{dM_{1450}}, \tag{12}$$

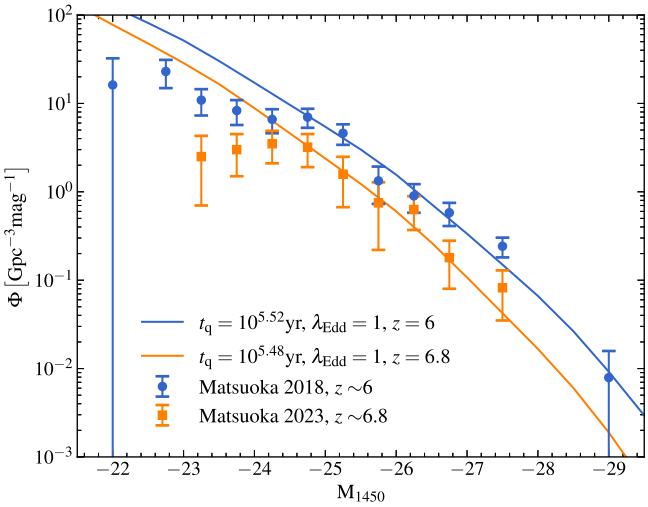

Figure 2. UV luminosity function fitting results. The average Eddington ratio of quasars is fixed at 1. The blue line represents $z = 6$, and the orange line represents $z = 6.8$. Solid lines represent the model best fits. Note that we ignored the first two points on the faint end during fitting due to observational incompleteness. The data points are provided by Y. Matsuoka et al. (2018) and Y. Matsuoka et al. (2023).

where $n_{\rm q}$ is the comoving number density of quasars, $dn_{\rm BH}/dM_{\rm BH}$ is the black hole mass function, and M_{1450} is the absolute magnitude at 1450 Å,

$$M_{1450} = -2.5 \log\left(\frac{L_\nu(\nu(1450\ \text{Å}))}{4\pi d^2 3631\ \text{Jy}}\right), \tag{13}$$

where $d = 10$ pc is expressed in centimeters.

In the calculation of QLF, $\lambda_{\rm Edd}$ and $t_{\rm q}$ are two parameters that are not strictly constrained by observations. Since both jointly determine the shape of QLF, they are strongly correlated parameters when fitting QLF to observations. Based on the discussion of the accretion rate in Section 2.3, we obtained the best fit to the observed luminosity function data by varying the average lifetime $t_{\rm q}$ of the quasars until χ^2 is minimized, using a fixed average Eddington ratio $\lambda_{\rm Edd} = 1$ for early quasars. We employed two sets of high-redshift observational data, obtained from observations of $z \sim 6$ (Y. Matsuoka et al. 2018) and $z \sim 6.8$ (Y. Matsuoka et al. 2023). Our best-fit results are shown in Figure 2. The reduced χ^2 obtained from the fits at $z = 6$ and $z = 6.8$ are 1.49 and 0.79, respectively. We take the logarithmic mean value $10^{5.5}$ yr in subsequent calculations. Note that both sets of data, especially the $z \sim 6.8$ data, are affected by incomplete observation coverage at the faint end, so we did not use the data points at the faint end with $M_{1450} > -24$ in the fitting process.

As a possible scenario, we also calculated the fit with an average Eddington ratio of $\lambda_{\rm Edd} = 1.2$, which is shown in Figure 3. The reduced χ^2 obtained from the fits at $z = 6$ and $z = 6.8$ are 1.26 and 0.68, respectively. From the results, it seems that the fits with a higher $\lambda_{\rm Edd}$ is better, but we must point out that this result could still be influenced by the incomplete observations of high-redshift QLF. The incompleteness effect can be divided into two parts. First, the sensitivity limitation, where there is incompleteness in the data at the faint end of QLF, and we mitigate this effect by discarding the data points with $M_{1450} > -24$. Second, the obscuration by the AGN dust torus may affect the completeness of optical observations,

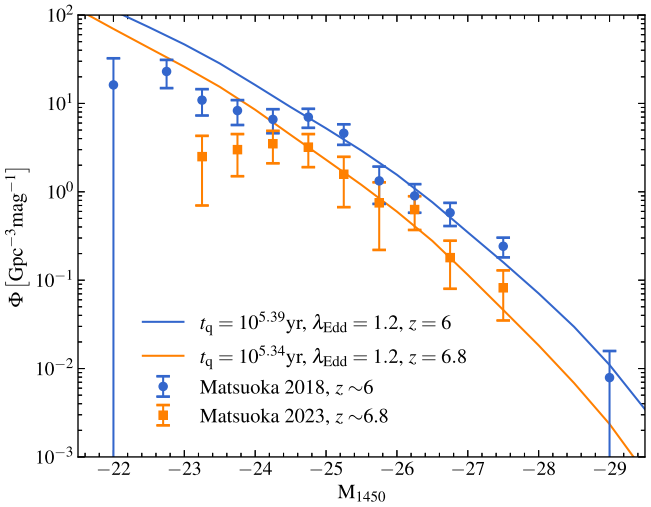

Figure 3. Similar to Figure 2, but the average Eddington ratio of quasars is fixed at 1.2.

meaning that some AGNs cannot be effectively detected in the optical band.

We note that F. Bolgar et al. (2018) used a constant duty cycle of $D_q = 0.02$ to fit the observed optical luminosity function. However, Z. Haiman & A. Loeb (1998) and M. G. Haehnelt et al. (1998) pointed out a connection between the duty cycle and Equation (4). If the amplitude factor A in Equation (4) is changed, the resulting duty cycle will also change. Since the amplitude factor A we use is different from that of F. Bolgar et al. (2018), the resulting duty cycle is also different. Note that our amplitude factor A and duty cycle D_q are fitted from observational data at $z \sim 6$, so the resulting duty cycle is only applicable to high redshifts.

2.5. Radio-loud Fraction

We assume that the radio-loud fraction (RLF) of quasars at high redshift is 10%. This assumption is consistent with observational studies of the RLF up to a redshift of $z \sim 6$ (D. Stern et al. 2000; Z. Ivezić et al. 2002; E. Bañados et al. 2015; A. J. Gloudemans et al. 2021; Y. Liu et al. 2021). We also note that L. Jiang et al. (2007) proposed a form for the evolution of the RLF with redshift and luminosity,

$$\log\left(\frac{\mathrm{RLF}}{1-\mathrm{RLF}}\right) = b_0 + b_z \log(1+z) + b_M (M_{2500} + 26), \tag{14}$$

where M_{2500} represents the optical magnitude at 2500 Å. b_0, b_z, and b_M are free parameters, with best-fit values of -0.132, -2.052, and -0.183, respectively. Since the recent study on the RLF of $z \geqslant 6$ quasars does not rule out the possibility of this form of evolution (P. M. Keller et al. 2024), we also calculated its impact on the results (see Section 3.6).

2.6. Radio-loudness Distribution

The radio-loudness distribution of AGNs shows a bimodal distribution in observations (e.g., P. A. Strittmatter et al. 1980; K. I. Kellermann et al. 1989; Z. Ivezić et al. 2002; R.L. White et al. 2007), suggesting the presence of two populations with different radio properties. The distribution can be well-fitted using two Gaussian components (e.g., M. Baloković et al. 2012; H. Xiao et al. 2022). In this study, we focus on the radio-loud population. We used the radio-loudness data of 225 radio-loud quasars with redshift from 0 to 5 from L. G. C. Bariuan et al. (2022) to perform a Gaussian fit of the radio-loudness distribution. The definition of radio-loudness is the logarithm of the ratio of the rest-frame luminosity between 5 GHz and 4400 Å ($R = \log_{10}(L_{5\mathrm{GHz}}/L_{4400})$). We estimate the radio-loudness distribution of the radio-loud quasars to be

$$N(R) = \frac{1}{\sqrt{2\pi}\,\sigma_0} \exp\left(\frac{-(R-\bar{R})^2}{2\sigma_0^2}\right), \tag{15}$$

where R is radio-loudness, and $\bar{R}$ and σ_0 are free parameters. Figure 4 shows the result of our radio-loudness distribution fitting, with the best-fit result being $\bar{R} = 2.67$ and $\sigma_0 = 0.55$. We also divided the data into four redshift bins for individual fitting,[8] with the results presented in Figure 5. As indicated, no

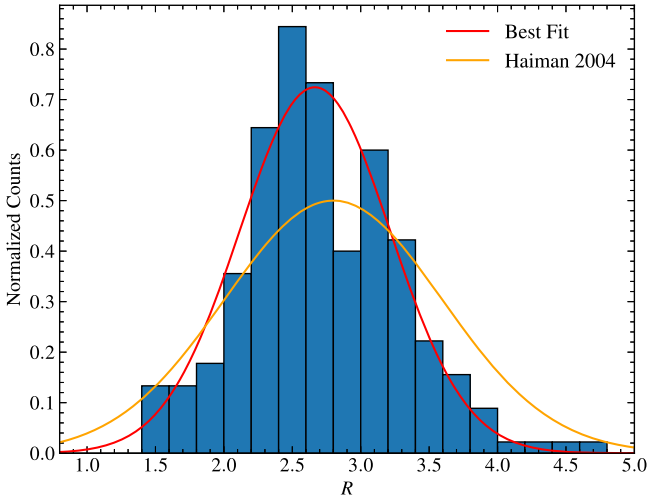

Figure 4. The fitting results of the radio-loudness distribution. The radio-loudness data used are from L. G. C. Bariuan et al. (2022). The red line represents our best fit to the data, and the orange line represents the radio-loudness distribution used in H04.

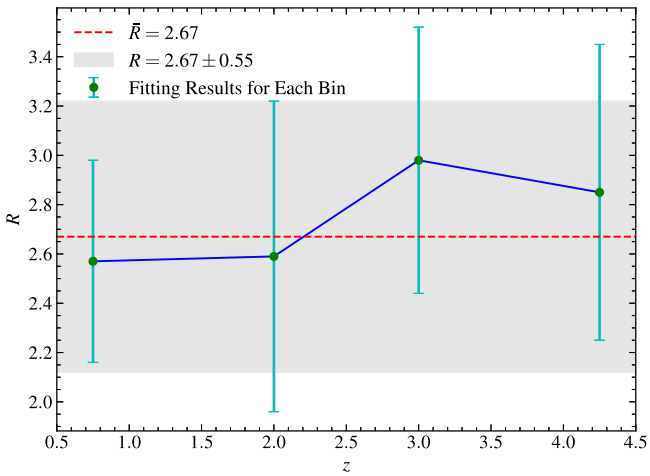

Figure 5. The radio-loudness fitting results for the four redshift bins. Green data points represent the means obtained from Gaussian fitting, with error bars indicating the σ_0 values. The red dashed line and shaded area denote the best fit, as depicted in Figure 4.

[8] The four redshift bins are [0, 1.5], (1.5, 2.5], (2.5, 3.5], and [3.5, 5].

significant redshift evolution is observed across the four bins. A separate Kolmogorov–Smirnov test (K-S test) was performed for every two redshift bins. All groups, except for the redshift range (2.5, 3.5], passed the K-S test. These results suggest that radio-loudness R either remains constant or exhibits only weak evolution with redshift z. Therefore, we believe that applying this distribution form to higher redshifts should be safe.

2.7. Radio Spectral Index

To calculate the radio luminosity of a particular band, we assume that the radio spectrum conforms to the following relation,

$$F_{\rm radio} \propto \nu^{\alpha}, \tag{16}$$

where $F_{\rm radio}$ is the radio flux and α is the radio spectral index. The radio spectral index affects two calculation processes: one involves converting from the observed frame to the rest frame, known as K-correction, and the other is the transformation between the 5 GHz definition of radio-loudness and the SKA-LOW observing band. Based on the findings of A. J. Gloudemans et al. (2021), who derived a median spectral index of -0.29 through the stacking of 93 quasars using the Low Frequency Array Two Meter Sky survey (LoTSS-DR2) and the Faint Images of the Radio Sky at Twenty Centimeters (FIRST) data, we adopt $\alpha = -0.29$. We also note that previous studies of high-redshift radio quasars used a steeper spectral index with $\alpha = -0.75$ (R. Wang et al. 2007; E. Bañados et al. 2015; Y. Liu et al. 2021), which is in agreement with very long baseline interferometry observations (S. Frey et al. 2005; E. Momjian et al. 2008; S. Frey et al. 2011; E. Momjian et al. 2018). Due to our limited understanding of high-redshift quasar radio spectra, we also calculated the impact of $\alpha = -0.75$ on the results as a possible scenario (see Section 3.5).

2.8. Radio-loud Quasar Abundance

Combining the above prescriptions, we can get the radio-loud quasar abundance with a radio flux density greater than a certain flux density threshold $F_{\rm threshold}$ as

$$\frac{dN}{dzd\Omega}(F_{\rm threshold}, z) = \frac{dV}{dzd\Omega} D_{\rm q} \times \int_0^{\infty} dM_{\rm halo} \left(\int_{R_0(M_{\rm halo}, F_{\rm threshold})}^{\infty} dR \quad N(R) \right) \frac{dn}{dM_{\rm halo}}, \tag{17}$$

where $dV/dzd\Omega$ is the cosmological volume element, R_0 is the threshold of radio-loudness calculated from the given radio flux density threshold $F_{\rm threshold}$ and halo mass $M_{\rm halo}$, duty cycle $D_{\rm q}$ can be found in Equation (11), radio-loudness distribution $N(R)$ can be found in Equation (15), and $dn/dM_{\rm halo}$ is the halo abundance calculated from Equations (1) and (2).

3. Results and Discussions

3.1. Quasar Abundance Predicted by the Model

Figure 6 shows the distribution of quasar abundance above a given radio flux density threshold as a function of redshift, obtained according to Equation (17). As discussed in Section 2, the standard parameter settings we used are as follows: average Eddington ratio $\lambda_{\rm Edd} = 1$, average quasar lifetime $t_{\rm q} = 10^{5.5}$ yr, radio spectral index $\alpha = -0.29$, and radio-loud fraction RLF = 10%.

3.2. Comparison with LOFAR Observations

We attempt to compare the calibrated model with existing high-redshift radio observations. Specifically, we use data from the ELAIS-N1 field in the LoTSS Deep Fields DR1 (J. Sabater et al. 2021; P. N. Best et al. 2023), which has the lowest average noise level in the three deep fields. We select radio-excess AGNs with redshifts between 5.6 and 6.4 from this deep field observation data and construct the radio luminosity function using the standard $1/V_{\rm max}$ technique (M. Schmidt 1968; J. J. Condon 1989). The details of the calculation and the incompleteness of information can be found in Section 3.1 of R. Kondapally et al. (2022). For our model, we convolve the optical luminosity function with the radio-loudness distribution to calculate the radio luminosity function. Figure 7 shows the comparison of the radio luminosity function predicted by our model with the LOFAR observations. At $z \sim 6$, the model-predicted radio luminosity function matches well with the LOFAR observations. However, we also notice that the observed radio luminosity function is slightly higher than the model prediction (within 1σ error range), and this discrepancy is more pronounced in the Lockman Hole field (about 1.58σ). Since our model is calibrated using the observed optical luminosity function, this discrepancy may indicate that some high accretion rate AGNs during the reionization epoch are optically obscured, similar to recently discovered high-redshift obscured AGNs (e.g., R. Endsley et al. 2023; E. Bañados et al. 2024; E. Lambrides et al. 2024). This suggests that the optical signals from certain AGNs cannot be effectively observed due to being obscured by dust, while their radio signals can still be detected. Therefore, the results provided by our model are conservative.

3.3. SKA-LOW Observation Forecast

For SKA-LOW radio-loud quasar observations, we considered two observation modes: the first is a survey to search for quasars. Since the goal of this survey is to find visible radio-loud quasars in the sky, a high-frequency resolution is not required, so we refer to it as a continuum survey. The relevant parameters for the continuum survey are summarized in Table 1. The second mode is a survey to find radio-loud quasars suitable for 21 cm forest studies. To resolve individual 21 cm lines, this survey requires higher frequency resolution, and thus we call it the 21 cm forest survey. The relevant parameters for the 21 cm forest survey are summarized in Table 2. Note that our 21 cm forest survey forecast shows the total number of sources within a survey area of 10,313 deg^2 that can resolve individual 21 cm lines with 100 hr of integration time. Conducting a 21 cm forest blind survey with this setup would require a substantial amount of observation time (~9 yr). From an observational perspective, we should first conduct the continuum blind survey to determine the positions of visible sources and then perform a high-frequency-resolution follow-up observations on those bright sources. How to filter high-redshift candidates from the blind survey is an important issue for future observations; we have performed the relevant discussions in Section 3.4.

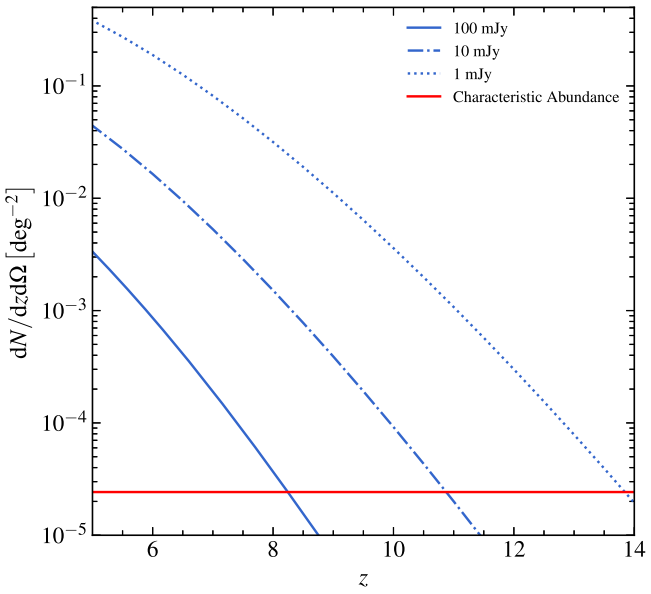

Figure 6. Predicted abundance of radio-loud quasars as a function of redshift, with different flux density thresholds at 150 MHz as indicated in the legend. The red line shows the characteristic abundance Φ^*, which corresponds to an abundance where the expected number of observations over the entire sky (~41,253 deg^2) is 1 ($\Phi^* \simeq 1/41253$ deg^{-2}). Sources with an abundance below this value are almost nonexistent.

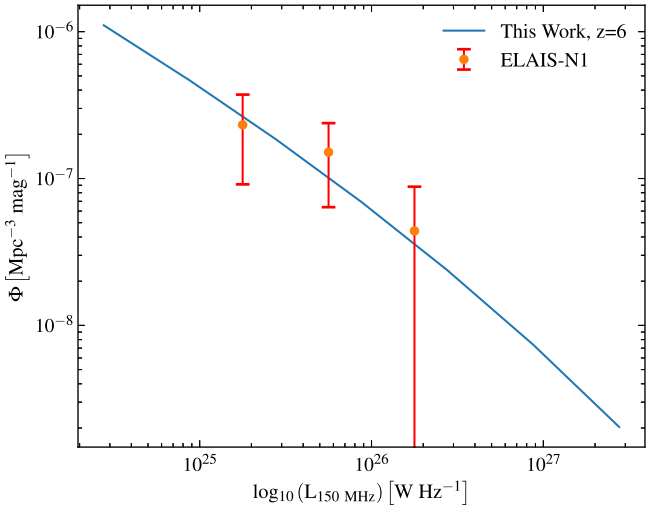

Figure 7. Comparison of the model-predicted radio luminosity function with observational data. The blue line represents the radio luminosity function of radio-loud quasars at $z = 6$ calculated by our model, while the red data points are the observational results from the ELAIS-N1 field in the LoTSS Deep Fields DR1, with error bars representing the 1σ error.

To predict the observations of SKA-LOW, we estimate the noise using the following formula (A. R. Thompson et al. 2017),

$$\delta S^N \approx \frac{2k_B T_{\rm sys}}{A_{\rm eff}\sqrt{2\delta\nu\delta t}}, \tag{18}$$

where $A_{\rm eff}$ is the effective collecting area of the telescope, $T_{\rm sys}$ is the system temperature, $\delta\nu$ is the channel width and δt is the integration time. For the continuum survey, the single-field integration time δt is determined by the survey coverage $S_{\rm tot}$

Table 1
Proposed Observation Parameters for SKA-LOW Continuum Survey

Parameter	Symbol	Value	Unit
Search Coverage	$S_{\rm tot}$	10,313	deg^2
Survey Time	$T_{\rm tot}$	365×6	hr
Effective Collecting Area	$A_{\rm eff}$	419,000	m^2
Channel Width	$\delta\nu$	10	MHz
Antenna Diameter	$D_{\rm ant}$	40	m
System Temperature	$T_{\rm sys}$	$40 + 1.1T_{\rm gal}$	K

Note. Instrument parameters are obtained from Square Kilometer Array Cosmology Science Working Group et al. (2020). The observation time is assumed to be 1 yr, and the effective observation time is 6 hr per day. $T_{\rm gal} = 25\left(\frac{408\ \mathrm{MHz}}{f(z)}\right)^{2.75}$, where $f(z)$ is the frequency at redshift z.

Table 2
Proposed Observation Parameters for SKA-LOW 21 cm Forest Survey

Parameter	Symbol	Value	Unit
Sky Coverage	$S_{\rm tot}$	10,313	deg^2
Integration Time	δt	100	hr
Effective Collecting Area	$A_{\rm eff}$	419,000	m^2
Channel Width	$\delta\nu$	5	kHz
Antenna Diameter	$D_{\rm ant}$	40	m
System Temperature	$T_{\rm sys}$	$40 + 1.1T_{\rm gal}$	K

Note. Similar to Table 1, the integration time and the channel width vary. See Section 3.3 for the observation strategy.

and the total survey time $T_{\rm tot}$,

$$\delta t = \frac{T_{\rm tot}}{S_{\rm tot}/\Omega}, \tag{19}$$

where Ω is the field of view, given by $\Omega \simeq (1.2\lambda/D_{\rm ant})^2$, in which $D_{\rm ant}$ is the diameter of a station. We estimate Ω using the wavelength corresponding to 150 MHz. We require the signal-to-noise ratio to be higher than 5 to detect quasars in a continuum survey, or to detect an absorption line for a follow-up 21 cm observation. For continuum surveys, this means flux density $> 5 \times \delta S^N$. For 21 cm forest surveys, we assume an optical depth of $\tau = 0.1$, as typical for absorption lines from minihalos or from the IGM with moderate heating during reionization (e.g., S. R. Furlanetto 2006; Y. Xu et al. 2011; B. Ciardi et al. 2013), which means flux density $> 5 \times \delta S^N/(1 - e^{-\tau})$.

Figures 8 and 9 show the model's predictions for 1 yr of SKA-LOW observations. At redshifts above 9, we expect to observe a large number of radio-loud quasars, among which approximately 20 quasars are bright enough to resolve individual 21 cm lines. This number of radio-loud quasars is enough to make the 21 cm forest an effective probe for the EOR. Note that we assume an effective daily observation time of 6 hr for the survey, which is a conservative estimate. Therefore, the actual number of quasars that can serve as 21 cm forest background sources is expected to be higher than our predictions.

3.4. Infrared Limit Estimation

For the actual observation of high-redshift quasars, obtaining redshift information is crucial. Currently, the search for quasars

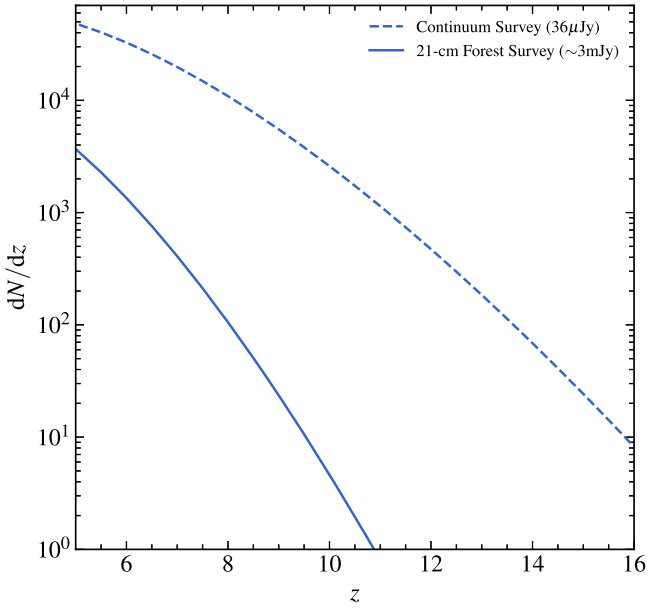

Figure 8. The number density of radio-loud quasars as expected in SKA-LOW observations. The dashed line represents the number density for a continuum survey, and the solid line represents the available bright sources for 21 cm forest observations. The sensitivity of the 21 cm forest survey shown in the figure corresponds to the flux density limit at $z = 9$, while at $z = 6$, the sensitivity is ~1.3 mJy. The parameters for the continuum survey and the 21 cm forest survey are shown in Tables 1 and 2, respectively.

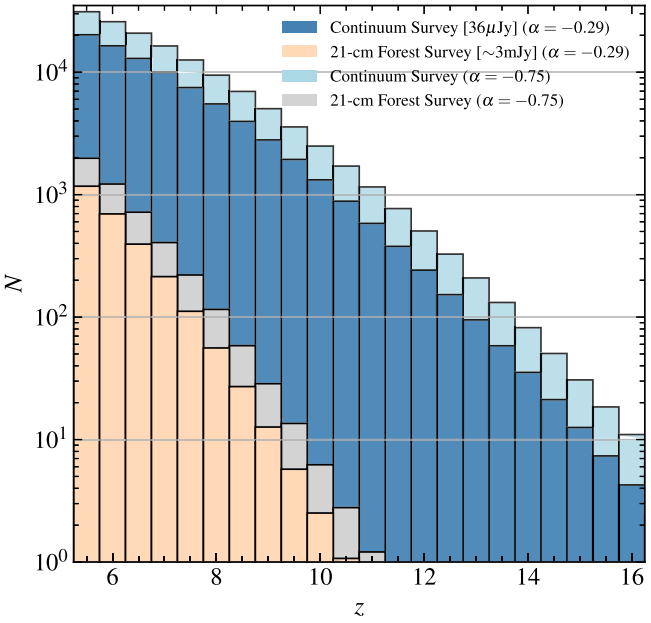

Figure 9. The integrated number of radio-loud quasars at various redshifts as expected in SKA-LOW observations. The darker blue and orange histograms are the results of the fiducial model with $\alpha = -0.29$, and the lighter blue and gray histograms represent the case where the radio spectral index $\alpha = -0.75$. The redshift bin width is 0.5. The sensitivity of the 21 cm forest survey shown in the figure corresponds to the flux density limit at $z = 9$, while at $z = 6$, the sensitivity is ~1.3 mJy.

primarily occurs in the optical and near-infrared bands. Candidate objects are selected through color–color diagram cuts (e.g., E. Bañados et al. 2016; L. Jiang et al. 2016; J. Yang et al. 2023; X. Lin et al. 2024), and redshift values are determined via photometric observations or spectral line identification. For the approximately 20 radio-loud quasars

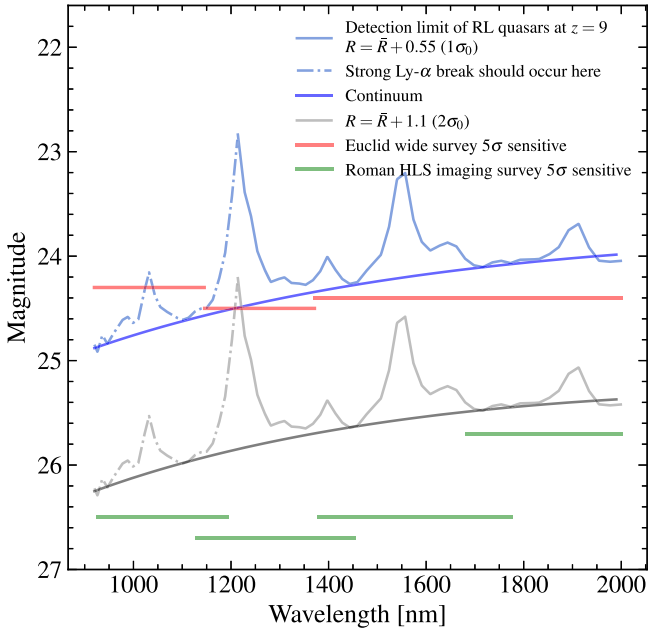

Figure 10. The infrared magnitude limit of quasars is required to have a radio flux density exceeding the threshold (~3 mJy at $z = 9$) for the 21 cm forest survey. The blue and gray lines represent quasars that exceed the average radio-loudness $\bar{R}$ by $1\sigma_0$ and $2\sigma_0$, respectively. The red and green lines correspond to the 5σ sensitivity of the Euclid and Roman Space Telescope surveys. The emission line structure is generated by the SED we used. Even quasars with extreme radio-loudness can be detected by future infrared surveys.

with $z \sim 9$ calculated in Section 3.3, the ideal detection method involves infrared-band photometric surveys, which provide redshift data through the identification of the Lyα break. While the JWST offers high sensitivity, it is not capable of conducting wide-field surveys. In contrast, current and future space-based infrared telescopes, such as Euclid (Euclid Collaboration et al. 2022) and the Nancy Grace Roman Space Telescope (Roman Space Telescope, D. Spergel et al. 2015), hold significant potential for such surveys.

Based on the radio flux density threshold for the 21 cm forest survey at $z = 9$ obtained in Section 3.3, we calculated the corresponding infrared AB magnitude threshold by considering radio-loudness and quasar SED. The results, along with the survey sensitivities of Euclid and Roman Space Telescope, are presented in Figure 10. Note that the emission line structure is based on the quasar SED we used, and we also fitted the shape of the continuum. As Figure 10 shows, Euclid can detect quasars with radio-loudness close to $\bar{R} + 1\sigma_0$ over a large survey area (~14,000 deg^2). In contrast, although the Roman Space Telescope covers a smaller area (~2200 deg^2), it can detect a small number of quasars with extreme radio-loudness ($R \gtrsim \bar{R} + 2\sigma_0$). Therefore, we believe that in the SKA era, combined with these infrared space telescopes, we can effectively search for high-redshift radio-loud quasars.

3.5. Influence of Radio Spectral Index

Figures 11 and 12 show the influence of different radio spectral indices on the results. Typically, we use -0.5 as a standard to determine whether a radio spectrum is steep or flat. Early radio studies of galaxies suggested a steep radio spectral index of -0.75 (J. J. Condon 1992), which has been adopted by multiple studies (e.g., R. Wang et al. 2007; E. Momjian et al. 2014; E. Bañados et al. 2015). We used the stacking result

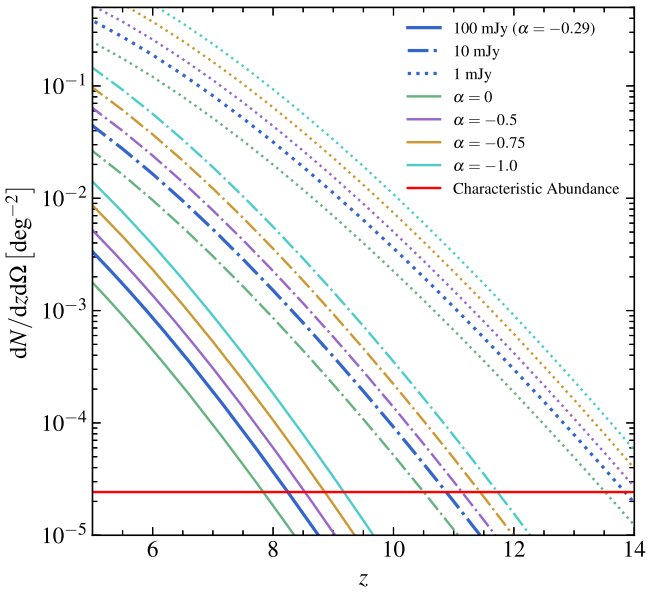

Figure 11. Influence of different radio spectral index settings on the abundance of radio-loud quasars. Different colors of lines represent different spectral indices, while different line styles represent different radio flux density thresholds (at 150 MHz). Sources with an abundance below the characteristic abundance marked by the red line are almost nonexistent.

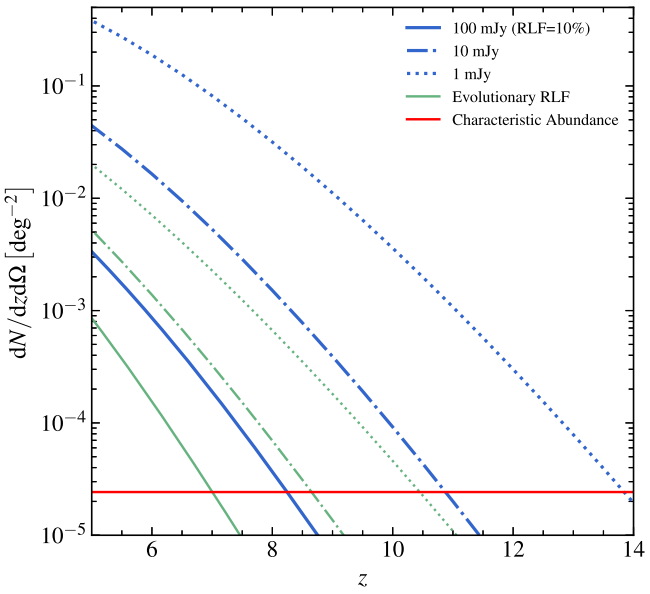

Figure 13. Influence of evolving RLF on the abundance of radio-loud quasars. The blue line represents a constant 10% RLF, while the green line represents an evolving RLF. Different line styles indicate different radio flux density thresholds (at 150 MHz). Sources with an abundance below the characteristic abundance marked by the red line are almost nonexistent.

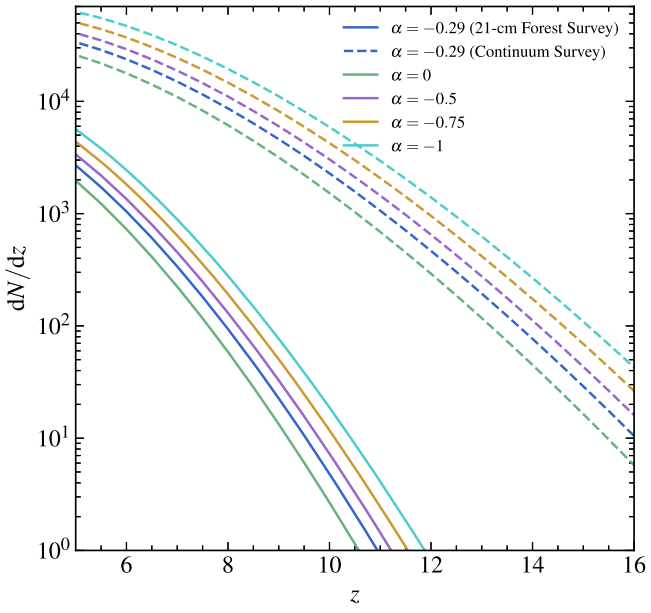

Figure 12. Influence of different radio spectral index settings on the forecast results of SKA-LOW observations. The observation frequency band of SKA-LOW is used for calculations here. Specifically, for the continuum surveys, we used 150 MHz, while for the 21 cm forest survey, we used the frequency of the redshifted 21 cm line.

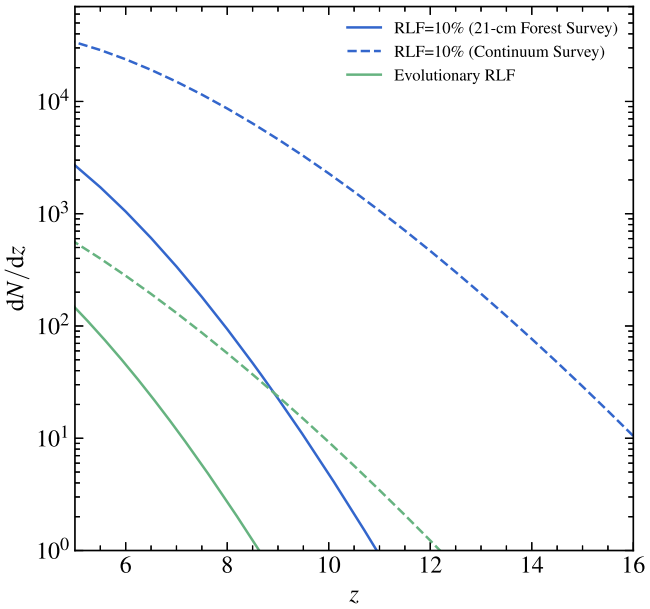

Figure 14. Influence of evolving RLF on the forecast results of SKA-LOW observations. The blue line represents a constant 10% RLF, while the green line represents an evolving RLF. The dashed line represents the continuum survey, and the solid line represents the 21 cm forest survey. Detailed descriptions of the continuum survey and the 21 cm forest survey can be found in Section 3.3.

of A. J. Gloudemans et al. (2021), $\alpha = -0.29$, as the standard parameter setting. However, it is noteworthy that the worse sensitivity of FIRST compared to LoTSS may naturally flatten the obtained spectral index. Since our understanding of the radio spectra of quasars is still limited, here we calculate the influence of multiple values of radio spectral indices on the results. As shown in Figures 11 and 12, our model indicates that a steeper spectral index is more beneficial for SKA-LOW's observations of high-redshift radio-loud quasars. This advantage arises because the radio-loudness R we are fitting is defined at 5 GHz, meaning that our results directly reflect the flux density at this frequency. A steeper radio spectrum produces stronger flux for sources within SKA-LOW's observation frequency range (50−350 MHz). The integral results suggest that adopting a steeper spectral index ($\alpha = -0.75$) instead of the flat spectral index proposed by A. J. Gloudemans et al. (2021) ($\alpha = -0.29$) could increase the

number of observable quasars at $z \sim 9$ by approximately 1.3 times (from 12 to 28). According to the requirements outlined by Y. Shao et al. (2023) for background sources in the 21 cm forest (10 quasars at $z = 9$), we anticipate sufficient background sources can be observed even with a flat spectral index. Consequently, the spectral index is not a critical parameter influencing the success of the 21 cm forest method.

3.6. Influence of Radio-loud Fraction

Figures 13 and 14 illustrate the impact of the evolution of RLF with redshift and luminosity on the results. We adopted the evolutionary form from L. Jiang et al. (2007), which implies that the RLF at high redshift is much lower than 10%. Under the assumption of evolutionary RLF, the model predicts a significant decrease in the abundance of quasars observable by SKA-LOW's 1 yr survey, making it more challenging to use the 21 cm forest method to probe cosmic reionization. If this RLF evolution is real, during the reionization period, the number of quasars with 100 hr integration times sufficient to resolve individual 21 cm lines is insufficient to support the 21 cm forest method, and we may need longer observation times to utilize relatively fainter quasars.

4. Conclusion

One of the interesting results obtained from our model is the average lifetime t_q of high-redshift ($z \gtrsim 6$) quasars. Assuming Eddington accretion, the observed high-redshift quasar luminosity function requires that the average lifetime of quasars given by the model is $\sim 10^{5.5}$ yr (see Section 2.4). Although this result is much smaller than early theoretical estimates ($\sim 10^7$ yr), it is close to recent constraints using Lyα near-zone data. Note that determining the average lifetime of quasars in the model requires a given halo–SMBH mass relationship, and currently, there is large uncertainty in the estimation of high-redshift SMBH and halo masses based on quasar spectra. It is foreseeable that with the accumulation of high-redshift observational data, our model can provide a more reliable average lifetime of quasars, which will help us understand the growth process of SMBHs in the early Universe.

Another notable finding concerns the accretion behavior of AGNs. Our model, calibrated at high redshift, resulted in a short quasar lifetime under the assumption of Eddington accretion. However, applying this setting to lower redshift results in significant discrepancies with observations. Additionally, we found that simply changing the quasar lifetime does not help, indicating that the assumption of quasars accreting at the Eddington rate at low redshifts is wrong. As a simple attempt, we recalibrated the model using the quasar luminosity function at $z = 4$ and allowed both $\lambda_{\rm Edd}$ and t_q to vary simultaneously, resulting in an average Eddington ratio of $\lambda_{\rm Edd} = 0.04$ and an average quasar lifetime of $t_q = 10^{8.2}$ yr. This suggests that the accretion behaviors of early and late AGNs differ greatly.

The most significant result derived from our model is the predicted abundance of radio-loud quasars observable by the SKA-LOW in a 1 yr survey. According to the standard parameter settings (Figure 8), we expect to identify over 1000 radio-loud quasars at $z > 6$ that are sufficient to resolve individual 21 cm lines, within a year of observation. Even at higher redshifts, such as $z > 9$, we can still detect approximately 20 such radio-loud quasars.

We tested the impact of various quasar radio spectral indices on our results (Figure 12). Our findings indicate that a steeper radio spectrum is more favorable for observations in the SKA-LOW frequency band. However, the radio spectral index is not a critical parameter influencing the success of the 21 cm forest method.

Our results indicate that whether RLF evolves is crucial for the observation of the 21 cm forest in the SKA era (Figure 14). If the RLF remains close to 10% at high redshift, then the 21 cm forest can serve as an effective probe of reionization. However, if the RLF evolution claimed by L. Jiang et al. (2007) is real, then it will be challenging to find background sources for detecting individual 21 cm absorption lines, and we may need longer integration times to utilize relatively fainter quasars. In this case, a statistical measurement of the 21 cm forest would be vital in alleviating the requirement on the brightness of background sources (K. J. Mack & J. S. B. Wyithe 2012; N. Thyagarajan 2020; Y. Shao et al. 2023).

Acknowledgments

We thank K. Shimasaku for providing us with the compiled data of the halo–SMBH mass relation. This work was supported by the National SKA Program of China (grant Nos. 2020SKA0110401, 2022SKA0110200, 2022SKA0110203, and 2020SKA0110100), the National Natural Science Foundation of China (grant Nos. 12473001, 11975072, 11875102, and 11835009), the National 111 Project (grant No. B16009), the CAS Project for Young Scientists in Basic Research (grant No. YSBR-092), the National Key R&D Program of China (grant No. 2022YFF0504300), and the science research grants from the China Manned Space Project (grant Nos. CMS-CSST-2021-B01 and CMS-CSST-2021-A02). LOFAR data products were provided by the LOFAR Surveys Key Science project (LSKSP; https://lofar-surveys.org/) and were derived from observations with the International LOFAR Telescope (ILT). LOFAR (M. P. van Haarlem et al. 2013) is the Low-Frequency Array designed and constructed by ASTRON. It has observing, data processing, and data storage facilities in several countries, which are owned by various parties (each with their own funding sources), and which are collectively operated by the ILT foundation under a joint scientific policy. The efforts of the LSKSP have benefited from funding from the European Research Council, NOVA, NWO, CNRS-INSU, the SURF Co-operative, the UK Science and Technology Funding Council, and the Jülich Supercomputing Center.

ORCID iDs

Qi Niu https://orcid.org/0009-0007-1168-0928
Yichao Li https://orcid.org/0000-0003-1962-2013
Yidong Xu https://orcid.org/0000-0003-3224-4125
Hong Guo https://orcid.org/0000-0003-4936-8247
Xin Zhang https://orcid.org/0000-0002-6029-1933

References

Baloković, M., Smolčić, V., Ivezić, Ž., et al. 2012, ApJ, 759, 30
Bañados, E., Mazzucchelli, C., Momjian, E., et al. 2021, ApJ, 909, 80
Bañados, E., Momjian, E., Connor, T., et al. 2024, NatAs, in press
Bañados, E., Schindler, J.-T., Venemans, B. P., et al. 2023, ApJS, 265, 29
Bañados, E., Venemans, B. P., Decarli, R., et al. 2016, ApJS, 227, 11
Bañados, E., Venemans, B. P., Morganson, E., et al. 2015, ApJ, 804, 118

Bariuan, L. G. C., Snios, B., Sobolewska, M., Siemiginowska, A., & Schwartz, D. A. 2022, MNRAS, 513, 4673
Best, P. N., Kondapally, R., Williams, W. L., et al. 2023, MNRAS, 523, 1729
Bolgar, F., Eames, E., Hottier, C., & Semelin, B. 2018, MNRAS, 478, 5564
Bowman, J. D., Rogers, A. E. E., Monsalve, R. A., Mozdzen, T. J., & Mahesh, N. 2018, Natur, 555, 67
Carilli, C. L., Gnedin, N. Y., & Owen, F. 2002, ApJ, 577, 22
Chatterjee, S., Elahi, K. M. A., Bharadwaj, S., et al. 2024, PASA, 41, e077
Chen, X., Yan, J., Xu, Y., et al. 2023, ChJSS, 43, 43
Ciardi, B., Inoue, S., Mack, K., Xu, Y., & Bernardi, G. 2015, in Proc. Advancing Astrophysics with the Square Kilometre Array (AASKA14), ed. T. L. Bourke et al. (Trieste: SISSA), 6
Ciardi, B., Labropoulos, P., Maselli, A., et al. 2013, MNRAS, 428, 1755
Condon, J. J. 1989, ApJ, 338, 13
Condon, J. J. 1992, ARA&A, 30, 575
de Lera Acedo, E., de Villiers, D.I.L., Razavi-Ghods, N., et al. 2022, NatAs, 6, 984
DeBoer, D. R., Parsons, A. R., Aguirre, J. E., et al. 2017, PASP, 129, 045001
Eilers, A.-C., Davies, F. B., Hennawi, J. F., et al. 2017, ApJ, 840, 24
Eilers, A.-C., Hennawi, J. F., Davies, F. B., & Simcoe, R. A. 2021, ApJ, 917, 38
Eisenstein, D. J., & Hu, W. 1999, ApJ, 511, 5
Endsley, R., Stark, D. P., Lyu, J., et al. 2023, MNRAS, 520, 4609
Euclid Collaboration, Scaramella, R., Amiaux, J., et al. 2022, A&A, 662, A112
Ferrarese, L. 2002, ApJ, 578, 90
Ferrarese, L., & Merritt, D. 2000, ApJL, 539, L9
Frey, S., Paragi, Z., Gurvits, L. I., Gabányi, K. É., & Cseh, D. 2011, A&A, 531, L5
Frey, S., Paragi, Z., Mosoni, L., & Gurvits, L. I. 2005, A&A, 436, L13
Furlanetto, S. R. 2006, MNRAS, 370, 1867
Furlanetto, S. R., & Loeb, A. 2002, ApJ, 579, 1
Furlanetto, S. R., Oh, S. P., & Briggs, F. H. 2006, PhR, 433, 181
Gebhardt, K., Bender, R., Bower, G., et al. 2000, ApJL, 539, L13
Gloudemans, A. J., Duncan, K. J., Röttgering, H. J. A., et al. 2021, A&A, 656, A137
Gloudemans, A. J., Duncan, K. J., Saxena, A., et al. 2022, A&A, 668, A27
Goulding, A.D., Greene, J. E., Setton, D. J., et al. 2023, ApJL, 955, L24
Gültekin, K., Richstone, D. O., Gebhardt, K., et al. 2009, ApJ, 698, 198
Gupta, Y., Ajithkumar, B., Kale, H. S., et al. 2017, CSci, 113, 707
Haehnelt, M. G., Natarajan, P., & Rees, M. J. 1998, MNRAS, 300, 817
Haiman, Z., & Loeb, A. 1998, ApJ, 503, 505
Haiman, Z., Quataert, E., & Bower, G. C. 2004, ApJ, 612, 698
Harikane, Y., Zhang, Y., Nakajima, K., et al. 2023, ApJ, 959, 39
Huynh, M., & Lazio, J. 2013, arXiv:1311.4288
Ighina, L., Belladitta, S., Caccianiga, A., et al. 2021, A&A, 647, L11
Ighina, L., Caccianiga, A., Moretti, A., et al. 2023, MNRAS, 519, 2060
Ivezić, Ž., Menou, K., Knapp, G. R., et al. 2002, AJ, 124, 2364
Jiang, L., Fan, X., Ivezić, Ž., et al. 2007, ApJ, 656, 680
Jiang, L., McGreer, I. D., Fan, X., et al. 2016, ApJ, 833, 222
Kadota, K., Sekiguchi, T., & Tashiro, H. 2021, PhRvD, 103, 023521
Keller, P. M., Thyagarajan, N., Kumar, A., Kanekar, N., & Bernardi, G. 2024, MNRAS, 528, 5692
Kellermann, K. I., Sramek, R., Schmidt, M., Shaffer, D. B., & Green, R. 1989, AJ, 98, 1195
King, A. 2003, ApJL, 596, L27
Kocevski, D. D., Onoue, M., Inayoshi, K., et al. 2023, ApJL, 954, L4
Kondapally, R., Best, P. N., Cochrane, R. K., et al. 2022, MNRAS, 513, 3742
Koopmans, L., Pritchard, J., Mellema, G., et al. 2015, in Proc. Advancing Astrophysics with the Square Kilometre Array (AASKA14), ed. T. L. Bourke et al. (Trieste: SISSA), 1
Kormendy, J., & Ho, L. C. 2013, ARA&A, 51, 511
Lambrides, E., Chiaberge, M., Long, A. S., et al. 2024, ApJL, 961, L25
Larson, R. L., Finkelstein, S. L., Kocevski, D. D., et al. 2023, ApJL, 953, L29
Li, W., Inayoshi, K., Onoue, M., & Toyouchi, D. 2023, ApJ, 950, 85
Lin, X., Wang, F., Fan, X., et al. 2024, ApJ, 974, 147
Liu, Y., Wang, R., Momjian, E., et al. 2021, ApJ, 908, 124
Lupi, A., Quadri, G., Volonteri, M., Colpi, M., & Regan, J.A. 2024, A&A, 686, A256
Lyu, J., Alberts, S., Rieke, G. H., et al. 2024, ApJ, 966, 229
Mack, K. J., & Wyithe, J.S.B. 2012, MNRAS, 425, 2988
Matsuoka, Y., Onoue, M., Iwasawa, K., et al. 2023, ApJL, 949, L42
Matsuoka, Y., Strauss, M. A., Kashikawa, N., et al. 2018, ApJ, 869, 150
McConnell, N. J., & Ma, C.-P. 2013, ApJ, 764, 184
McGreer, I. D., Becker, R. H., Helfand, D. J., & White, R. L. 2006, ApJ, 652, 157
Momjian, E., Carilli, C. L., Bañados, E., Walter, F., & Venemans, B. P. 2018, ApJ, 861, 86
Momjian, E., Carilli, C. L., & McGreer, I. D. 2008, AJ, 136, 344
Momjian, E., Carilli, C. L., Walter, F., & Venemans, B. 2014, AJ, 147, 6
Monsalve, R. A., Altamirano, C., Bidula, V., et al. 2024, MNRAS, 530, 4125
Morales, M. F., & Wyithe, J. S. B. 2010, ARA&A, 48, 127
Morey, K. A., Eilers, A.-C., Davies, F. B., Hennawi, J. F., & Simcoe, R. A. 2021, ApJ, 921, 88
Munshi, S., Mertens, F. G., Koopmans, L. V. E., et al. 2024, A&A, 681, A62
Navros, O. 2022, PhD thesis, Carnegie Mellon Univ.
Pacucci, F., Ferrara, A., Volonteri, M., & Dubus, G. 2015, MNRAS, 454, 3771
Parsons, A. R., Backer, D. C., Foster, G. S., et al. 2010, AJ, 139, 1468
Patil, A. H., Yatawatta, S., Koopmans, L. V. E., et al. 2017, ApJ, 838, 65
Philip, L., Abdurashidova, Z., Chiang, H. C., et al. 2019, JAI, 8, 1950004
Planck Collaboration, Aghanim, N., Akrami, Y., et al. 2020, A&A, 641, A6
Price, D. C., Greenhill, L. J., Fialkov, A., et al. 2018, MNRAS, 478, 4193
Pritchard, J. R., & Loeb, A. 2012, RPPh, 75, 086901
Runnoe, J. C., Brotherton, M. S., & Shang, Z. 2012, MNRAS, 422, 478
Sabater, J., Best, P. N., Tasse, C., et al. 2021, A&A, 648, A2
Sathyanarayana Rao, M., Singh, S., K. S., S., et al. 2023, ExA, 56, 741
Schmidt, M. 1968, ApJ, 151, 393
Shang, Z., Brotherton, M. S., Wills, B. J., et al. 2011, ApJS, 196, 2
Shao, Y., Xu, Y., Wang, Y., et al. 2023, NatAs, 7, 1116
Sheth, R. K., & Tormen, G. 2002, MNRAS, 329, 61
Shimabukuro, H., Ichiki, K., Inoue, S., & Yokoyama, S. 2014, PhRvD, 90, 083003
Shimabukuro, H., Ichiki, K., & Kadota, K. 2020, PhRvD, 101, 043516
Shimasaku, K., & Izumi, T. 2019, ApJL, 872, L29
Silk, J., & Rees, M.J. 1998, A&A, 331, L1
Singh, S., Subrahmanyan, R., Udaya Shankar, N., et al. 2018, ApJ, 858, 54
Šoltinský, T., Bolton, J. S., Hatch, N., et al. 2021, MNRAS, 506, 5818
Šoltinský, T., Bolton, J. S., Molaro, M., et al. 2023, MNRAS, 519, 3027
Spergel, D., Gehrels, N., Baltay, C., et al. 2015, arXiv:1503.03757
Square Kilometre Array Cosmology Science Working Group, Bacon, D. J., Battye, R. A., et al. 2020, PASA, 37, e007
Stern, D., Djorgovski, S. G., Perley, R. A., de Carvalho, R. R., & Wall, J.V. 2000, AJ, 119, 1526
Strittmatter, P. A., Hill, P., Pauliny-Toth, I.I.K., Steppe, H., & Witzel, A. 1980, A&A, 88, L12
Sun, T.-Y., Shao, Y., Li, Y., Xu, Y., & Zhang, X. 2024, arXiv:2407.14298
Thompson, A. R., Moran, J. M., & Swenson, G.W.J. 2017, Interferometry and Synthesis in Radio Astronomy (3rd ed.; Berlin: Springer),
Thyagarajan, N. 2020, ApJ, 899, 16
Tingay, S. J., Goeke, R., Bowman, J. D., et al. 2013, PASA, 30, e007
Übler, H., Maiolino, R., Curtis-Lake, E., et al. 2023, A&A, 677, A145
van Haarlem, M. P., Wise, M. W., Gunst, A. W., et al. 2013, A&A, 556, A2
Wang, F., Yang, J., Fan, X., et al. 2021, ApJL, 907, L1
Wang, R., Carilli, C. L., Beelen, A., et al. 2007, AJ, 134, 617
White, R. L., Helfand, D. J., Becker, R. H., Glikman, E., & de Vries, W. 2007, ApJ, 654, 99
Willott, C. J., Delorme, P., Reylé, C., et al. 2010, AJ, 139, 906
Wyithe, J. S. B., & Loeb, A. 2003, ApJ, 595, 614
Xiao, H., Zhu, J., Fu, L., Zhang, S., & Fan, J. 2022, PASJ, 74, 239
Xu, Y., Chen, X., Fan, Z., Trac, H., & Cen, R. 2009, ApJ, 704, 1396
Xu, Y., Ferrara, A., & Chen, X. 2011, MNRAS, 410, 2025
Xu, Y., Ferrara, A., Kitaura, F. S., & Chen, X. 2010, SCPMA, 53, 1124
Xu, Y., & Zhang, X. 2020, SCPMA, 63, 270431
Yang, J., Wang, F., Fan, X., et al. 2021, ApJ, 923, 262
Yang, J., Fan, X., Gupta, A., et al. 2023, ApJS, 269, 27
Zubovas, K., & King, A. 2021, MNRAS, 501, 4289